Journal of Materials Chemistry A

PAPER

View Article Online
View Journal | View Issue

Cite this: J. Mater. Chem. A, 2024, 12, 7896

Nickel single atom mediated phosphate functionalization of moss derived biochar effectively enhances electrochemical uranium extraction from seawater†

Huachuan Feng,‡[a] Huanhuan Dong,‡[a] Pan He,‡[b] Junhui He,[c] Enmin Hu,[a] Zishu Qian,[a] Jin Li,[a] Jiejie Li,[a] Wenkun Zhu *[a] and Tao Chen *[a]

Electrochemical uranium extraction is considered a promising approach to obtain uranium resources from seawater. Here, we report an electrocatalyst composed of single-atom Ni located at *R. japonicum* L. biomass derived carbon with phosphate modification (Ni–BC@PO_4) for efficient electrochemical uranium extraction from seawater. By virtue of density functional theory (DFT) calculations, it was confirmed that the synergistic effect of the single-atom Ni and phosphate modification in the *R. japonicum* L. biomass derived carbon significantly enhances the capture of UO_2^{2+} and accelerates the electron transfer to the captured UO_2^{2+}, thereby accelerating the reaction kinetics of uranium electrochemical extraction. As a result, Ni–BC@PO_4 demonstrates excellent uranium extraction capability (2.86 mg g^{-1} d^{-1}) in real seawater. Relying on various spectroscopic techniques, we further confirm that the captured uranyl ions undergo a continuous and complex reaction process, being captured by phosphate groups, electron reduced, reoxidized by oxidizing radicals, and recrystallized with Na^+ in solution to generate an $Na_2O(UO_3{\cdot}H_2O)_x$ precipitate. Furthermore, Ni–BC@PO_4 demonstrates outstanding antibacterial and corrosion resistance. This study provides an example for designing advanced electrocatalysts with highly active centers and strong capturing capabilities for uranium extraction, offering theoretical guidance for seawater uranium resource extraction technology.

Received 24th November 2023
Accepted 30th January 2024

DOI: 10.1039/d3ta07267c

rsc.li/materials-a

1 Introduction

With the continuous growth of global energy demand and the promotion of renewable energy, nuclear power has received significant attention as a clean and efficient energy option.[1,2] Traditional uranium ore mining faces various challenges,[3] such as ore scarcity and environmental damage.[4] In comparison, the amount of uranium resources in seawater is enormous, approximately 4500 times that of land-based uranium resources.[1,5,6] Therefore, extracting uranium from seawater undoubtedly offers a pathway with immense potential and economic value. Traditional physical adsorbents, such as metal oxides/sulfides,[7] nano zero-valent iron particles,[8] biomass derivatives (amyloid-like proteinaceous[9]), and porous biomass carbon-based materials,[10] have been explored as potential adsorbents for uranium extraction from seawater.[11,12] However, they still face challenges such as poor selectivity and limited specific functional groups and active sites. Consequently, designing and developing novel and efficient extraction technologies for uranium extraction from seawater can contribute to the acquisition of uranium resources in seawater.

Recently, the electrochemical extraction method has gained widespread attention as a low-cost, efficient, and sustainable technique for uranium enrichment in seawater. It demonstrates excellent uranium enrichment capability while avoiding the need for large-scale waste disposal.[13–16] For example, Cui *et al.*[17] developed a half-wave rectification alternating current electrochemical method for uranium extraction from seawater, greatly improving the selectivity and adsorption kinetics of uranium at specific voltages. In the latest research, biomass carbon has been utilized as a catalyst for electrochemical uranium extraction due to its wide availability, low cost, high surface area, and specific three-dimensional pore structure.[18,19] However, the limited electrochemical active centers and uranium

[a]State Key Laboratory of Environment-friendly Energy Materials, National Co-innovation Center for Nuclear Waste Disposal and Environmental Safety, Sichuan Co-Innovation Center for New Energetic Materials, Nuclear Waste and Environmental Safety Key Laboratory of Defense, School of Life Science and Engineering, Southwest University of Science and Technology, Mianyang, Sichuan 621010, P. R. China. E-mail: zhuwenkun@swust.edu.cn; chent@swust.edu.cn

[b]College of Chemistry, Key Laboratory of Radiation Physics & Technology, Ministry of Education, Sichuan University, Chengdu, Sichuan 610064, P. R. China

[c]Department of Materials Engineering, Sichuan College of Architectural Technology, Sichuan 618000, P. R. China

† Electronic supplementary information (ESI) available. See DOI: https://doi.org/10.1039/d3ta07267c

‡ These authors contributed equally to this work.

coordination sites, as well as the biological damage to the catalysts by seawater, hinder their application in seawater uranium extraction.[20–22] Previous studies have found that loading single-atom active sites onto carbon materials to form metal–nitrogen–carbon (M–N–C) structures, resembling porphyrins, can significantly enhance the electrocatalytic performance and antibacterial properties of the catalysts.[15,23,24] The coordination of nickel with nitrogen to form Ni–N_x effectively enhances electron transfer,[25] and the anchoring of Ni–N_4 by porous biomass carbon further enhances this charge transfer process.[26] Parallel to the construction of single-atom active sites, tailoring the coordination environment of catalysts with specific functional groups such as acyl oxime, hydroxyl, carboxylic acid, and particularly phosphoric acid groups can significantly increase the uranium binding ability of the catalysts, thus achieving high uranium extraction efficiency.[27–29] Therefore, tailoring biochar-based catalysts with single-atom active centers and surface phosphate modification holds the potential for achieving efficient electrochemical uranium extraction from seawater.

In this work, we report for the first time a nickel single atom loaded moss biochar catalyst with a phosphorylated surface (Ni–BC@PO_4) for electrochemical uranium extraction. Accordingly, Ni–BC@PO_4 exhibited an excellent U(vi) extraction capacity of 137.8 mg g^{-1} for uranium in spiked seawater at 8 ppm concentration. More importantly, Ni–BC@PO_4 was able to extract approximately 28.6 μg of uranium (enrichment capacity of approximately 2.86 mg g^{-1} d^{-1}) from 10 L of natural seawater (initial uranium concentration ≈ 3.3 ppb) within 24 hours. By virtue of DFT calculations, we have confirmed that the functionalization of phosphoric acid effectively enhances the capture of uranyl ions, with nickel single atom active centers serving as the main electron transport hub for uranium reduction. Subsequent mechanistic studies indicated that the UO_2^{2+} ions captured by the phosphate group in Ni–BC@PO_4 were reduced to U(IV) *via* the nickel monoatomic active center, and finally oxidized and recrystallized again to generate an $Na_2O(UO_3 \cdot H_2O)_x$ precipitate with the aid of $^{\cdot}O_2^-$ and $^{\cdot}OH$. Furthermore, the Ni–BC@PO_4 demonstrates excellent reusability, antibacterial properties, and corrosion resistance. This work not only provides a new perspective for the development of catalysts for electrochemical seawater uranium extraction, but also proposes new scenarios for studying the electrochemical evolution process of uranium.

2 Materials and methods

2.1 Synthesis of BC and Ni–BC

First of all, dry *R. japonicum* L. powder was crushed and sieved through a 60 mesh filter, then 1 g of biomass and 1 g of potassium carbonate powder were dissolved in 10 mL of deionized water and magnetically stirred for 10 hours. The resulting sample was then centrifuged, dried, and carbonized for 2 hours at 450 °C in a nitrogen environment, resulting in a black powder named BC. The nickel precursor material was obtained by dispersing 5 g of $C_2H_4N_2$ and 0.5 g of $NiCl_2 \cdot 6H_2O$ in 100 mL of deionized water, stirring for 12 hours, and then vacuum drying for 12 hours at 550 °C in an air atmosphere. Subsequently, 1 g of nickel material was loaded onto 1 g of BC using a ball mill, and carbonized for 2 hours at 700 °C in a nitrogen atmosphere with a heating rate of 10 °C min^{-1}, resulting in a product named Ni–BC.

2.2 Phosphorylation modification of Ni–BC@PO_4 and BC@PO_4

0.2 g of Ni–BC was added to 150 mL of deionized water in a beaker, and stirred until it dispersed before slowly adding 2 mL of a 70% phytic acid solution and ultrasonicating for 20 minutes. The mixed solution was then transferred to a 200 mL PTFE-lined reactor and stored for 12 hours at 95 °C. The resulting solution was centrifuged at 8000 rpm for 5 minutes at room temperature, and then washed three times with deionized water and anhydrous ethanol. Finally, the material was dried under vacuum at 60 °C for 12 hours to obtain Ni–BC@PO_4. The synthesis method for BC@PO_4 is identical to that of Ni–BC@PO_4, with the only difference being the substitution of BC for Ni–BC.

2.3 Characterization

Multiple material characterization methods and instruments were used to characterize the prepared materials. The ESI† includes detailed descriptions and assessments of the characterization process.

3 Results and discussion

3.1 Material design concept: single-atom loading and surface phosphoric acid modification

Before the synthesis of Ni–BC@PO_4, state-of-the-art DFT simulations were carried out first to determine whether integrating single atom nickel and surface phosphate modification can alter the binding ability of biochar to uranyl ions (Fig. 1). First of all, to better understand the effect of Ni single-atoms and surface phosphoric acid groups on the electronic properties of biochar, we conducted DFT calculations by utilizing a graphene slab with hydroxyl groups/phosphoric acid groups (C_6–OH and Ni SAc–C_6–PO_4) (Fig. 1a and b). Compared with C_6–OH, the phosphoric acid groups on the Ni SAc–C_6–O–P were more electronegative, which is beneficial for the extraction of uranium due to the soft hard acid–base theory. After the capture of uranyl ions, the nickel single atom transfers high-density electrons to the phosphate groups through C–O–P bridging bonds for the catalytic reduction of the uranyl ions. Additionally, we further calculated the adsorption energy (E_{ads}) of the uranyl ion on both models. The E_{ads} of the uranyl ion on Ni SAc–C_6–PO_4 was −6.695 eV, significantly lower than the E_{ads} on C_6–OH (−4.584 eV), further proving the preferential anchoring effect of phosphate groups.

3.2 Characterization results of the catalysts

Inspired by DFT calculations, we propose a single atom Ni loading and surface phosphate modification strategy to enhance the electrochemical uranium extraction performance

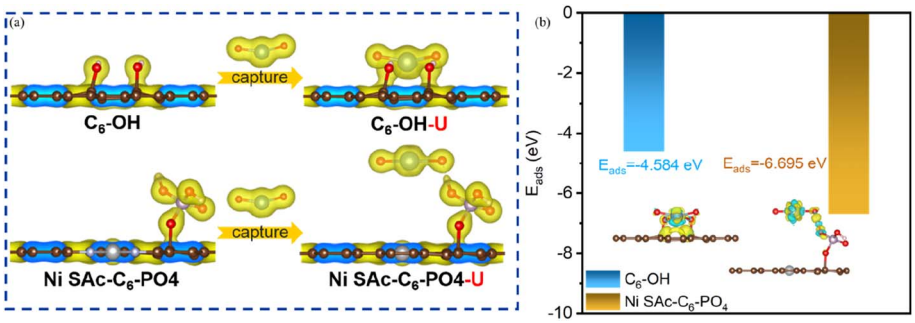

Fig. 1 (a) Adsorption model of uranyl ions in the system without/with phosphoric acid modification (side view). (b) Electron density difference and E_{ads}.

of biomass derived carbon. Fig. 2a illustrates the detailed synthesis process of Ni–BC@PO_4. First of all, a continuous high-temperature calcination strategy was employed to construct atomically dispersed Ni single-atom active centers (referred to as Ni–BC) anchored on porous biomass carbon derived from *R. japonicum* L. Subsequently, hydrothermal grafting of phosphoric acid groups led to the synthesis of Ni–BC@PO_4. In the synthesis strategy, *R. japonicum* L. biomass carbon (Fig. S3†) with high specific surface area and abundant porous structure can anchor nickel atoms in the precursor of nickel cyanide (Ni–CN) through strong metal–support interactions, while simultaneously achieving self-nitrogen doping. According to Lewis acid–base theory, the introduction of phosphate groups provides the catalyst with better hydrophilicity and UO_2^{2+} capturing capability. In accordance with inductively coupled plasma optical emission spectroscopy (ICP-OES) results, the loading of Ni in Ni–BC@PO_4 was determined to be 0.98%. The specific surface area and pore size distribution of a material are important factors affecting its performance. Through BET testing, it was found that the prepared Ni–BC@PO_4 has a high specific surface area of 668 $m^2\ g^{-1}$ and an average pore size of 7.38 nm (Fig. S2†). Additionally, the nitrogen adsorption–desorption isotherms of Ni–BC@PO_4 are shown in Fig. S1.† The morphology of Ni–BC@PO_4 was characterized using scanning electron microscopy (SEM). The results showed that after annealing and hydrothermal treatment, the prepared Ni–BC@PO_4 maintained its original porous structure (Fig. S4†). As shown by transmission electron microscopy (TEM), Ni–BC@PO_4 exhibited a nanosheet-like morphology (Fig. 2b). As shown in the X-ray powder diffraction (XRD) patterns (Fig. 2d and S6†), no characteristic diffraction peaks of nickel species were observed during the further annealing and phosphoric acid modification processes. Only a broad peak caused by the (002) plane of graphitic carbon at 24.8° was observed, consistent with the TEM results mentioned above.[30] The distribution of single-atom Ni sites was further confirmed *via* aberration-corrected high-angle annular dark-field scanning transmission electron microscopy (AC-TEM). The bright clusters of dots indicated by red circles in Fig. 2c represent Ni atoms. Due to the significant Z-contrast difference between Ni and N/C atoms, the atomic dispersion of Ni atoms on the biomass carbon substrate can be clearly observed. Moreover, energy-dispersive X-ray spectroscopy (EDS) mapping analysis revealed the uniform distribution of Ni, C, N, O, and P throughout the structure (Fig. S5†), confirming the successful synthesis of single-atom Ni and functionalization with phosphate groups.

Synchrotron X-ray absorption spectroscopy (XAS) was further employed to investigate the chemical state and coordination information of Ni atoms in Ni–BC@PO_4. The normalized X-ray absorption near edge structure (XANES) spectrum of Ni–BC@PO_4 is observed between the spectra of metallic nickel foil and nickel oxide, indicating the oxidation state of Ni in Ni–BC@PO_4 is between 0 and +2 (ref. 31) (Fig. 2e). It is noteworthy that the Fourier-transformed extended X-ray absorption fine structure (EXAFS) spectrum of Ni–BC@PO_4 in Fig. 2f displayed a predominant peak at ≈1.31 Å, without the detection of the Ni–Ni peak at ≈2.18 Å observed in the nickel foil and avoiding overlap with the Ni–O peak at ≈1.62 Å in nickel oxide.[32] The above results indicated that Ni species exist in the form of atomically dispersed Ni single atoms, either as Ni–N or Ni–C. Furthermore, the N 1s signal of BC (Fig. S7†) revealed that nitrogen element mainly exists in the form of pyrrolic nitrogen (398.5 eV) and pyridinic nitrogen (400.1 eV) in BC. In contrast, the N 1s XPS spectra of Ni–BC and Ni–BC@PO_4 (Fig. S8†) exhibited characteristic peaks corresponding to the Ni–N (~399.5 eV) bond and the graphitic nitrogen (401.3 eV) bond, with a shift of the pyridinic nitrogen binding energy (400.3 eV) to a higher value by 0.2 eV.[33] This can be explained by the utilization of the coordination ability of pyridinic nitrogen to form a stable Ni–N bond by BC and the precursor of nickel during the annealing process.[34] Additionally, based on the C 1s XPS spectra fitting results of Ni–BC and Ni–BC@PO_4 (Fig. S9†), no new bonds were generated during the annealing and modification processes, further confirming that the Ni single atoms were anchored *via* Ni–N bonds rather than Ni–C bonds. Moreover, a least-squares EXAFS curve fitting analysis (Fig. 2g) was performed to obtain quantitative structural data of Ni–BC@PO_4. The best-fit analysis revealed a coordination number of 4 for Ni–N and an average bond length of 1.98 Å. Further atomic distribution of Ni–BC@PO_4 was revealed by EXAFS wavelet transform analysis. As shown in Fig. 2h, the maximum intensities of the Ni metal and NiO references appeared at ~7.9 and ~7.3 $Å^{-1}$, respectively. More importantly,[35] Ni–BC@PO_4 exhibited a maximum intensity at ~5.2 Å, distinct from the Ni–

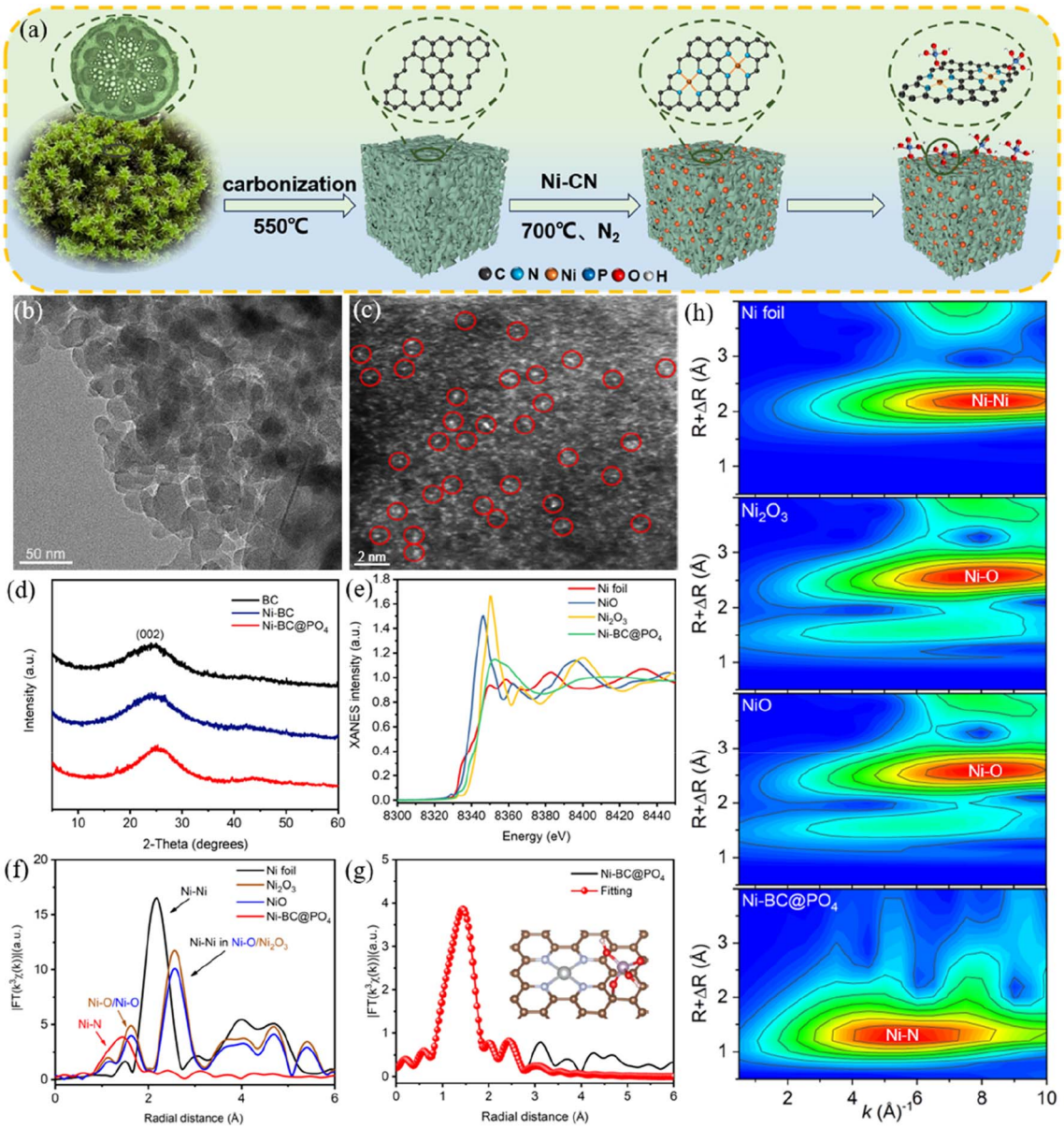

Fig. 2 (a) Process flowchart of Ni–BC@PO_4. (b) TEM image of Ni–BC@PO_4. (c) AC-TEM image of Ni–BC@PO_4. (d) XRD patterns of BC, Ni–BC, and Ni–BC@PO_4. (e) Comparison of the normalized XANES spectra of Ni–BC@PO_4 at the Ni K-edge with Ni foil, Ni_2O_3, and NiO references. (f) Corresponding k^2-weighted Fourier transform of the EXAFS spectra. (g) EXAFS r space-fitting curves. (h) Corresponding wavelet transforms.

Ni and Ni–O bonds. The above evidence suggests that Ni species exist in the form of atomically dispersed single atoms, and one Ni atom is anchored to phosphoric acid-modified nitrogen-doped porous biomass carbon through quadruple coordination with N atoms (Ni–N_4).

Fourier-transform infrared spectroscopy (FT-IR) and X-ray photoelectron spectroscopy (XPS) were employed to reveal the changes in elemental composition and structural properties during the synthesis of Ni–BC@PO_4. The FT-IR spectrum shown in Fig. S10† exhibited characteristic peaks at 3401, 1586, and 1388 cm^{-1}, corresponding to the O–H, C=O, and C–OH functional groups,[28] respectively, indicating the retention of the oxygen-containing functional groups of biomass carbon (BC) in Ni–BC and Ni–BC@PO_4. Additionally, the FT-IR spectrum of Ni–BC@PO_4 displayed the stretching vibration peaks of P–O (1048 cm^{-1}) and P=O (1163 cm^{-1}) groups,[29] suggesting the phosphate groups had been successfully modified in Ni–BC@PO_4, which is conducive to the capture of uranyl ions. Correspondingly, the P 2p XPS spectrum showed the presence of (Fig. S11†) P=O (134.71 eV) and P–O (133.86 eV) bonds, which is attributed to the introduction of phosphate groups. Furthermore, the C 1s spectrum of Ni–BC@PO_4 displayed a 0.2 eV shift towards lower binding energy for the C–O bond, indicating the successful grafting of phosphoric acid groups onto the carbon substrate *via* C–O–P bridging.[36] The Ni 2p XPS spectrum of Ni–BC@PO_4 (Fig. S12†) exhibited characteristic

peaks corresponding to Ni $2p_{3/2}$ and Ni $2p_{1/2}$, indicating the successful loading of Ni single atoms during the upstream material preparation process and the effective retention of Ni single atoms during the downstream phytic acid modification process.[33] Based on the above analysis, we can confirm that the nickel atoms are successfully anchored on the biomass carbon derived from moss in an atomically dispersed Ni–N_4 structure, while the phosphate groups are successfully grafted onto the carbon substrate through stable C–O–P bridges.

3.3 Catalyst performance evaluation

Firstly, we evaluated the physical-chemical adsorption performance of Ni–BC@PO_4 towards uranium. With the grafting of phosphate groups, Ni–BC@PO_4 demonstrated a uranium enrichment capacity of 20.2 mg g^{-1} at room temperature. Its uranium enrichment ability showed a synchronous change with temperature and reached 26.9 mg g^{-1} at 303 K, and the adsorption process followed pseudo-first and pseudo-second order kinetic models[37] (Fig. S13†). Additionally, in the presence of multiple coexisting ions, Ni–BC@PO_4 exhibited a distribution coefficient for uranium of 237.5 mL g^{-1}, significantly higher than that of other ions (Fig. S14†). Inspired by the well-defined Ni single-atom active centers, we conducted uranium extraction experiments using a three-electrode system with Ag/AgCl as the reference electrode. BC, Ni–BC, and Ni–BC@PO_4 were used as working electrodes in 0.5 M Na_2SO_4 solution with a uranium concentration of 8 ppm in simulated seawater. Fig. 3a shows the U(VI) extraction curves of BC, Ni–BC, BC@PO_4, and Ni–BC@PO_4 over time. After 50 minutes, the U(VI) removal rates of BC@PO_4 and Ni–BC reached 27.05% and 32.18% respectively, showing higher removal rates compared to pristine BC (20.93%). Meanwhile Ni–BC@PO_4 exhibited a much higher removal rate of 51.69%, about 2.5 times that of pristine BC. As the reaction progressed to 400 min, the U(VI) extraction rates of Ni–BC and Ni–BC@PO_4 were 85.65% and 91.73% respectively, significantly higher than those of pristine BC (47.66%) and BC@PO_4 (53.53%). This result demonstrated that the introduction of phosphate groups and Ni single-atom active centers can effectively enhance the electrochemical extraction efficiency of uranium. To further evaluate the reaction kinetics, the apparent rate constants were calculated using a pseudo-first-order kinetic model for different materials. The fitting results (Fig. 3b) showed that the k values followed the order of Ni–BC@PO_4 (0.00508) > Ni–BC (0.00458) > BC@PO_4 (0.00157) > BC (0.00105), indicating that the introduction of single-atom active centers and the functionalization with phosphoric acid accelerated the reaction kinetics of electrochemical uranium extraction, leading to improved uranium extraction efficiency. Subsequently, linear sweep voltammetry (LSV) tests were performed in simulated seawater with 8 mg per g U(VI). The spectra (Fig. S15†) showed a peak at −0.36 V for Ni–BC@PO_4, corresponding to the reduction peak of uranium, while the uranium reduction peaks for Ni–BC and BC were observed around

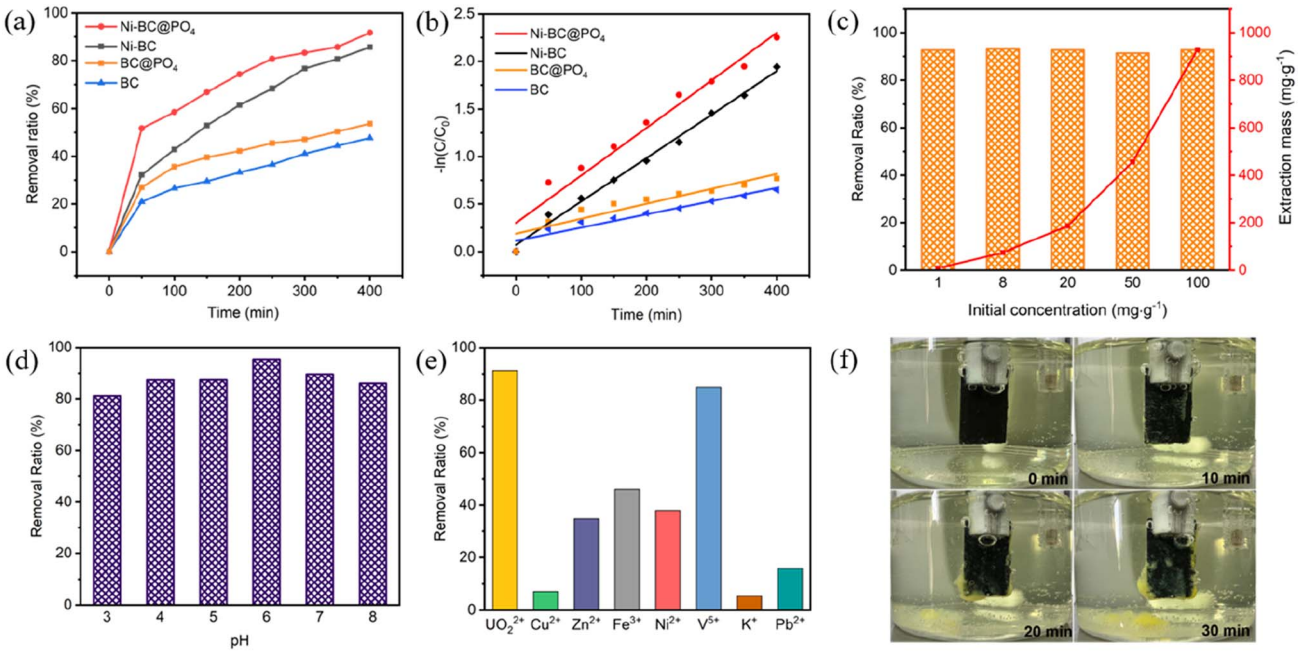

Fig. 3 (a) Removal efficiency of U(VI) *versus* time for BC, BC@PO_4, Ni–BC, and Ni–BC@PO_4. ($V = -1.8$ V, $C_{U(VI)} = 8$ mg L^{-1}, $m/V = 0.1$, $T = 293$ K, pH = 5.5). (b) Fitting curves for the time curves of electrochemical uranium extraction using BC, BC@PO_4, Ni–BC, and Ni–BC@PO_4. (c) Removal efficiency and enrichment capacity of U(VI) by Ni–BC@PO_4 under different initial concentrations. ($V = -1.8$ V, $C_{U(VI)} = 1$ mg L^{-1}, 8 mg L^{-1}, 20 mg L^{-1}, 50 mg L^{-1} and 100 mg L^{-1}, $m/V = 0.1$, $T = 293$ K, pH = 5.5). (d) Electrochemical uranium extraction performance of Ni–BC@PO_4 under different pH conditions. ($V = -1.8$ V, $C_{U(VI)} = 8$ mg L^{-1}, $m/V = 0.1$, $T = 293$ K, pH = 3, 4, 5, 6, 7 and 8). (e) Uranium extraction performance of Ni–BC@PO_4 under multi-ion coexistence. ($V = -1.8$ V, $C_{U(VI)} = 8$ mg L^{-1}, $C_{K(I)} = 400$ mg L^{-1}, the concentration of other interfering ions is consistent with that of uranium, $m/V = 0.1$, $T = 293$ K, pH = 5.5). (f) Electrochemical uranium extraction process of Ni–BC@PO_4 in a 500 ppm uranium solution within 0-30 minutes. ($V = -1.8$ V, $C_{U(VI)} = 500$ mg L^{-1}, $m/V = 0.1$, $T = 293$ K, pH = 5.5).

−0.41 V and −0.74 V, respectively. This result indicates that the introduction of nickel single-atom active sites and phosphate groups effectively lowers the reduction potential of uranium, facilitating uranium reduction. Furthermore, we evaluated the reusability of Ni–BC@PO_4 by performing repetitive U(VI) electrochemical cycles, and Ni–BC@PO_4 maintained an excellent U(VI) removal rate of 85% after five cycles (Fig. S16†). Subsequently, we characterized the Ni–BC@PO_4 after five cycles using XRD, FT-IR, and AC-TEM, confirming the excellent stability of nickel single atoms (Fig. S17–S19†).

Electrochemical uranium extraction is often influenced by various factors. To explore the efficiency of electrochemical extraction in different U(VI) environments, batch electrochemical uranium extraction experiments were conducted under different concentrations, pH levels, and coexisting ions. As shown in Fig. 3c, Ni–BC@PO_4 exhibited significant U(VI) removal rates at initial concentrations ranging from 1 to 100 mg L^{-1}. Specifically, the U(VI) concentration decreased from 1 mg L^{-1} to 73 μg L^{-1} within 400 min. At an initial uranium concentration of 100 mg L^{-1}, Ni–BC@PO_4 achieved a uranium extraction capacity of 927.66 mg g^{-1}. The chemical state of uranium is closely related to the pH of the environment. Therefore, we conducted uranium extraction experiments in simulated seawater with pH ranging from 3 to 8. The results showed that Ni–BC@PO_4 maintained a high removal efficiency of U(VI) at different pH levels (Fig. 3d). To further observe the impact of pH, we used Visual MINTEQ 3.1 to simulate the changes in uranium species in the above-mentioned solution (Fig. S20†). At pH = 3, the presence of SO_4^{2-} in the solution formed UO_2SO_4 and $UO_2(SO_4)_2^{2-}$ complexes with some UO_2^{2+} ions, resulting in a relatively low removal rate of only 81.1% for Ni–BC@PO_4. As the pH increased, the uranium species gradually transformed to $(UO_2)_3(OH)_5^+$, and the competition diminished. At pH = 6, Ni–BC@PO_4 achieved the highest removal rate of U(VI) at 95.41%. Furthermore, various cations (Cu^{2+}, Zn^{2+}, Fe^{3+}, Ni^{2+}, V^{5+}, Pb^{2+}, Mg^{2+}, and Ca^{2+} at 8 mg g^{-1} and K^+ at 400 mg g^{-1}) and anions (F^-, CO_3^{2-}, NO_3^-, and Cl^- at 0.1 M) were individually added to the U(VI) solution to explore their effects on the electrochemical uranium extraction using Ni–BC@PO_4. Ni–BC@PO_4 demonstrated excellent uranium extraction capacity in the presence of these ions (Fig. S21 and S22†). As shown in Fig. 3e, the uranium extraction capability of Ni–BC@PO_4 in the presence of multiple coexisting cations was also studied. Ni–BC@PO_4 once again demonstrated its potential for uranium extraction from seawater with an excellent U(VI) extraction rate of 91.2%. To visually observe the electrochemical uranium extraction process of Ni–BC@PO_4, electrochemical extraction experiments were conducted with an initial uranium concentration of 500 mg L^{-1}. Images of uranium deposits on the Ni–BC@PO_4 electrode were captured at t = 0, 10, 20, and 30 minutes. As clearly observed in Fig. 3f, the uranium species in the solution rapidly evolved into a large amount of easily separable yellow precipitate on the electrode surface, and the accumulated precipitate became significantly thicker with increasing time.

3.4 Application of the catalysts in seawater

The properties of the material itself, such as hydrophilicity, resistance to biological damage, *etc.*, usually play a crucial role in the efficiency of uranium electrochemical separation. To further verify its feasibility in seawater, we first evaluated the hydrophilicity of the material. As shown in Fig. 4a, the introduction of phosphate groups in Ni–BC@PO_4 enhanced the affinity between the catalyst and water compared to Ni–BC, effectively improving the collision between the catalyst and uranyl ions, facilitating the capture of uranium by the material. Equally important is the susceptibility of the electrode material to bacterial corrosion in seawater. In other words, the antimicrobial performance of the material directly affects its catalytic performance and application. As shown in the images in Fig. 4b, under light, when *E. coli*, *Pseudomonas*, and marine bacteria were co-cultured with a concentration of 1 mg per mL BC, the inhibition of bacteria by BC was only 35%. It is worth noting that the co-culture with Ni–BC, loaded with single nickel atoms, resulted in a significant increase in the inhibition rates of *E. coli*, marine bacteria, and *Pseudomonas*, with nearly complete inhibition of marine bacteria (91.4% inhibition rate). Furthermore, after phosphate modification, Ni–BC@PO_4 demonstrated enhanced antibacterial activity. We visually demonstrated the antibacterial effects of BC and Ni–BC@PO_4 using the line streak method (Fig. S23†). To observe the antibacterial activity of Ni–BC@PO_4 in real seawater uranium extraction, a Laser Scanning Confocal Microscope (LSCM) was used to examine the surface of Ni–BC@PO_4 before and after the reaction in seawater. The results (Fig. 4c) showed that initially, bacteria were randomly distributed on the surface of Ni–BC@PO_4 in seawater, but after electrochemical uranium extraction, almost all bacterial cell membranes exhibited rupture, with disrupted cell morphology and significantly reduced bacterial activity. This difference in antimicrobial properties is attributed to the nickel single-atom loading, which gives the material better resistance to biological corrosion. Subsequently, the presence of a significant amount of reactive oxygen species (ROS), including hydroxyl radicals and superoxide radicals, was detected on Ni–BC@PO_4 through electron spin resonance (ESR) testing (Fig. 4d and e). The antimicrobial mechanism is illustrated in Fig. 4h. When oxygen was activated by electrons at the active nickel single-atom sites, $^{\bullet}O_2^-$ and $^1O_2$ were produced. Additionally, due to electron consumption, the remaining holes reacted with H_2O or OH^- to form $^{\bullet}OH$.[23,29] The generation of these reactive oxygen species accelerated the decomposition of cellular organic components, thereby inhibiting bacterial growth.

Based on the above characteristics and the excellent performance of Ni–BC@PO_4 in simulated seawater, the application of Ni–BC@PO_4 in spiked and real seawater uranium extraction was further investigated using a three-electrode system. The uranium extraction rate of Ni–BC@PO_4 in 8 ppm spiked seawater is shown in Fig. 4f. Within the first 2 hours, the uranium removal rate reached a very high 53.2%. As the reaction continued to 7 hours, the uranium removal rate experienced another turning point,

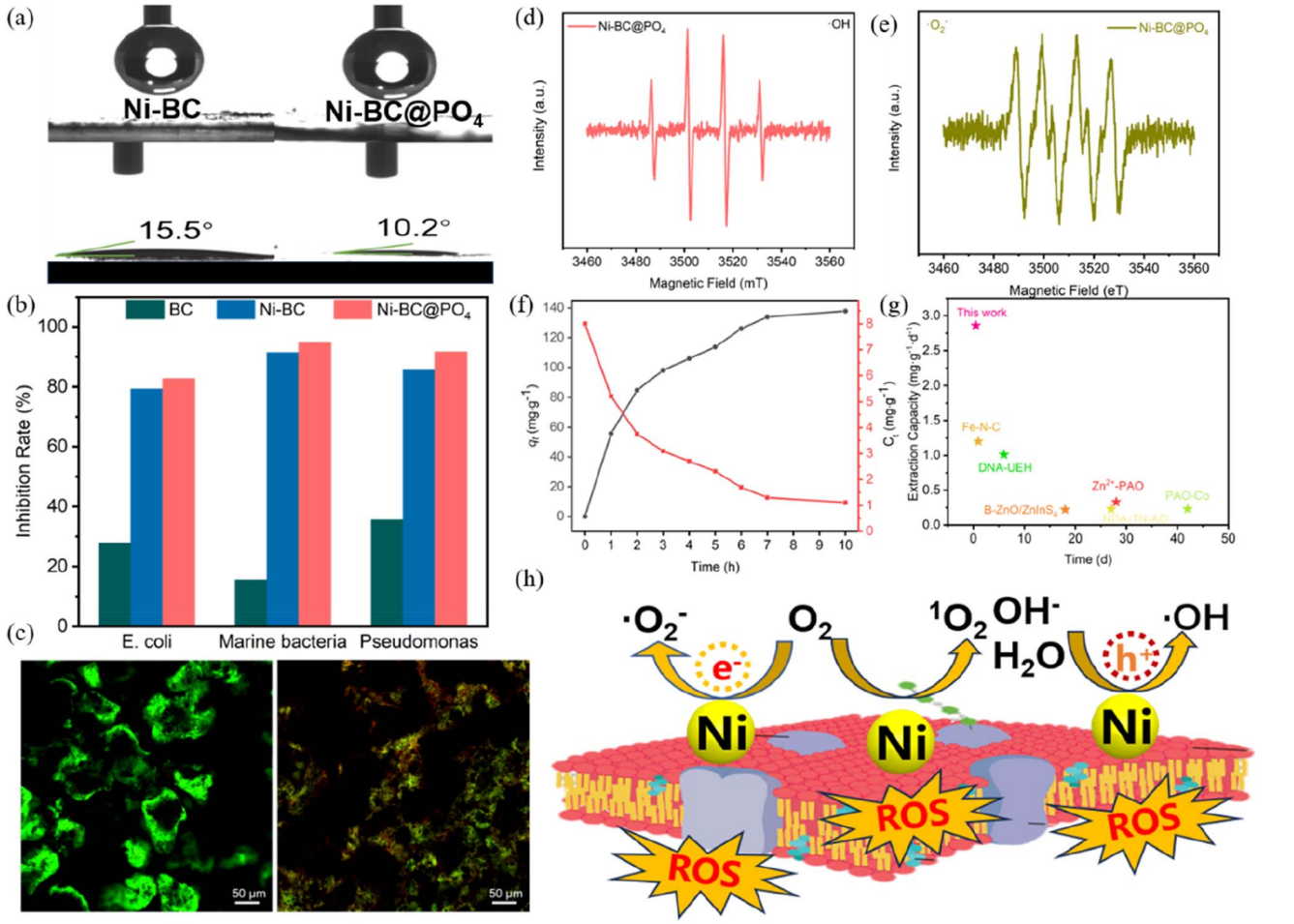

Fig. 4 (a) Water contact angle of Ni–BC and Ni–BC@PO_4. (b) Inhibition rate of BC, Ni–BC, and Ni–BC@PO_4. (c) Laser Scanning Confocal Microscope (LSCM) images of bacteria staining before and after the Ni–BC@PO_4 reaction. (d and e) ESR spectra of the Ni–BC@PO_4–U. (f) Electrochemical uranium extraction time curve of Ni–BC@PO_4 in seawater spiked with 8 ppm uranium. ($V = -1.8$ V, $C_{U(VI)} = 8$ mg L^{-1}, $m/V = 0.1$, $T = 293$ K, pH = 7.5). (g) The comparison of carbon's actual uranium extraction capability in seawater with that of other materials. (h) Antibacterial mechanism diagram of Ni–BC@PO_4.

reaching 83.7% at that time. In the last 3 hours, the leaching rate of uranium plateaued, which is attributed to the reduction of UO_2^{2+} captured by phosphate groups and the reduced effective communication between the electrode and uranyl ions. The maximum uranium enrichment capacity reached 137.84 mg g^{-1} in 8 ppm spiked seawater. Lastly, but most importantly, we evaluated the uranium extraction capability of Ni–BC@PO_4 in a 10 L real seawater system by continuously extracting for 24 hours at a voltage of −1.8 V (Fig. 4g). Afterwards, the electrode was subjected to a reverse voltage of 1.8 V in 20 mL of 0.1 M HCl for analysis, resulting in a uranium concentration of up to 1.43 μg mL^{-1} in the solution. This means that 28.6 μg of uranium was extracted from 10 L of seawater, achieving an enrichment capacity of 2.86 mg g^{-1} d^{-1}. This capacity is much higher than that of previously reported electrochemical seawater uranium extraction materials. Subsequently, we roughly estimated the cost of the electrochemical seawater uranium extraction method to be $264 per kg. For specific details, please refer to Table S2.†

3.5 Electrochemical uranium extraction mechanism

To investigate the extraction mechanism of uranium in the Ni–BC@PO_4, the catalyst was observed using TEM after uranium extraction. As shown in Fig. S24,† Ni–BC@PO_4–U maintained its original amorphous sheet-like structure after electrochemical uranium extraction. Significant amounts of needle-shaped substances appeared on the surface of Ni–BC@PO_4, which may be attributed to the formation of new uranium species (Fig. 5a). Elemental mapping revealed that the deposits were mainly composed of U, O, and Na, providing direct evidence that the deposits belong to a uranium oxide compound (inset in Fig. 5a and S25†). Furthermore, in the high-resolution transmission electron microscopy (HRTEM) image of Ni–BC@PO_4–U, a lattice spacing of 0.32 nm corresponding to the (030) plane of $Na_2O(UO_3 \cdot H_2O)_x$ (PDF # 12-0112) was observed (Fig. 5b), providing strong evidence that uranyl ions receiving electrons delivered from Ni single-atom active centers and ultimately transform into $Na_2O(UO_3 \cdot H_2O)_x$ precipitates. As shown in the X-ray powder diffraction pattern of Ni–BC@PO_4–U (Fig. 5c), new

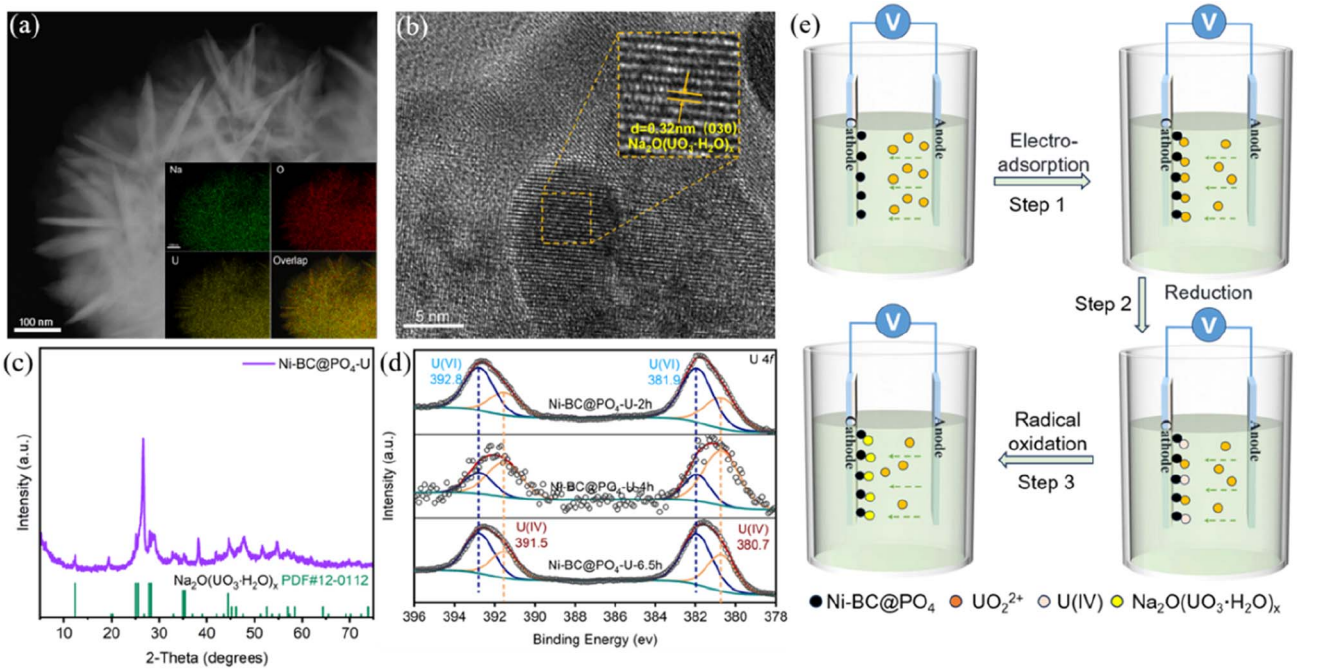

Fig. 5 (a) TEM image of Ni–BC@PO_4–U. (b) HRTEM image of Ni–BC@PO_4–U. (c) XRD pattern of Ni–BC@PO_4–U. (d) The U 4f XPS spectra of Ni–BC@PO_4–U at 2 h, 4 h, and 6.5 h. (e) Process diagram for electrochemical extraction of uranium by Ni–BC@PO_4.

characteristic diffraction peaks appeared at 12.36°, 25.09°, 25.57°, 27.83°, and 28.31°, corresponding to the (100), (200), (021), (030), and (121) planes of $Na_2O(UO_3 \cdot H_2O)_x$, respectively.[22] This indicates that the above deposits belong to $Na_2O(UO_3 \cdot H_2O)_x$. Meanwhile, the U=O stretching vibration peak of U(VI) at approximately 885 cm^{-1} (ref. 8 and 38) also appeared in the FT-IR spectrum of Ni–BC@PO_4–U (Fig. S26†), while there are alterations in the signals of P=O and P–O bonds, implying the interaction between the phosphate groups and uranium as the primary trapping sites for uranyl ions.[39] In the XPS fine spectrum of U 4f for Ni–BC@PO_4–U after 2 hours of electrochemical uranium extraction, signals of U(IV) and U(VI) appeared at 380.7 eV(IV), 391.5 eV (VI), 381.9 eV (IV), and 392.8 eV (VI),[40,41] confirming the occurrence of a reduction reaction from U(VI) to U(IV) (Fig. 5d). When the reaction progressed to 4 hours, the proportion of U(VI) to U(IV) was significantly lower, indicating a substantial conversion of U(VI) to U(IV). Importantly, when the reaction reached 6.5 hours, the content of U(VI) became higher than that of U(IV) again, indicating a reverse process from U(IV) to U(VI).

Based on the previous free radical tests, we have reason to believe that the re-oxidation of uranium species is associated with free radicals. Taking all the analyses into consideration, we infer that the captured uranyl ions undergo a continuous and complex reaction process, being captured by phosphate groups, electron reduced, reoxidized by oxidizing radicals, and recrystallized with Na^+ in solution to generate $Na_2O(UO_3 \cdot H_2O)_x$. The possible steps of the reaction are as follows:

$$U(VI) + e_{Ni-BC@PO_4}^- \rightarrow U(IV) \quad (1)$$

$$H_2O \rightarrow O_2 + H^+ + e^- \quad (2)$$

$$H_2O + h^+ \rightarrow {}^{\cdot}OH + h^+ \quad (3)$$

$$O_2 + e_{Ni-BC@PO_4}^- \rightarrow {}^{\cdot}O_2^- \quad (4)$$

$$U(IV) + {}^{\cdot}O_2^- + {}^{\cdot}OH + Na^+ \rightarrow Na_2O(UO_3 \cdot H_2O)_x \quad (5)$$

Fig. 5e depicts the complete sequence of the reaction process. The UO_2^{2+} in the solution migrates towards the cathode under the driving force of an external electric field, while the phosphate groups on Ni–BC@PO_4 capture a large amount of free UO_2^{2+}. Following that, the captured U(VI) receives electrons from the nickel single-atom active centers and undergoes reduction to U(IV). Simultaneously, the oxygen in the aqueous solution system receives electrons and is reduced to $^1O_2$ and $^{\cdot}O_2^-$. The remaining holes then react with H_2O to produce $^{\cdot}OH$. Finally, under the action of $^{\cdot}OH$ and $^{\cdot}O_2^-$, the reduced U(IV) is oxidized again and combines with Na^+ ions to form a precipitate of $Na_2O(UO_3 \cdot H_2O)_x$.

4 Conclusion

In conclusion, the photocatalytic activity and selective reduction of uranium were effectively enhanced by constructing Ni–BC@PO_4. The Surface phosphate modification endows Ni–BC@PO_4 with excellent hydrophilicity and high affinity for uranyl ions, while the nickel single-atom active center dominates electron transfer in the uranium reduction reaction, significantly enhancing the electro-assisted uranium extraction activity of Ni–BC@PO_4. The batch experimental results show that Ni–BC@PO_4 exhibits an extraction capacity of 2.86 mg g^{-1}

d^{-1} in real seawater. Furthermore, Ni–BC@PO_4 maintains excellent interference resistance and antibacterial properties in the presence of multiple ions and in highly biologically active environments. Mechanistic studies have shown that the captured uranyl ions undergo a continuous and complex reaction process, being captured by phosphate groups, electron reduced, reoxidized by oxidizing radicals, and recrystallized with Na^+ in solution to generate an $Na_2O(UO_3 \cdot H_2O)_x$ precipitate. This work provides a new approach for the rational design of advanced electrocatalysts for extracting uranium resources from seawater, as well as an original approach for studying the evolution mechanism of uranium species.

Data availability

The datasets used or analyzed during the current study are available from the corresponding author on reasonable request.

Author contributions

Huachuan Feng: conceptualization, methodology, investigation, writing – original draft preparation, writing – review & editing; Huanhuan Dong: writing – original draft preparation; Pan He: software; resources. Junhui He: methodology; Enmin Hu: validation, methodology; Zishu Qian: validation, Jin Li: methodology; Jiejie Li: methodology; Wenkun Zhu: funding acquisition, resources. Tao Chen: project administration, supervision; writing – review & editing.

Conflicts of interest

The authors declare that they have no known competing financial interests or personal relationships that could have appeared to influence the work reported in this paper.

Acknowledgements

This work was supported by NSFC (No. 21976147, 22206142, and U2267224), Sichuan Science and Technology Program (No. 23NSFSC0838 and 2022YFG0371), the Open Fund of CNNC Key Laboratory for Uranium Extraction from Seawater (KLUES202201), the Project of State Key Laboratory of Environment-friendly Energy Materials in SWUST (No. 21fksy22), and the Research Fund of SWUST for PhD (No. 23zx7110 and 22zx7175). The authors would like to thank Shiyanjia Lab (**https://www.shiyanjia.com**) and Suzhou Deyo Bot Advanced Materials Co., Ltd. (**https://www.szdybc.com**) for providing support with material characterization.

References

1 M. Keener, C. Hunt, T. G. Carroll, V. Kampel, R. Dobrovetsky, T. W. Hayton and G. Ménard, *Nature*, 2020, **577**, 652–655.
2 S. Mollick, S. Saurabh, Y. D. More, S. Fajal, M. M. Shirolkar, W. Mandal and S. K. Ghosh, *Energy Environ. Sci.*, 2022, **15**, 3462–3469.
3 D. Mei, H. Li, L. Liu, L. Jiang, C. Zhang, X. Wu, H. Dong and F. Ma, *Chem. Eng. J.*, 2021, **425**, 130468.
4 Y. Li, Y. Zheng, Z. Ahamd, L. Zhu, J. Yang, J. Chen and Z. Zhang, *Coord. Chem. Rev.*, 2023, **491**, 215234.
5 Y. Xie, Z. Liu, Y. Geng, H. Li, N. Wang, Y. Song, X. Wang, J. Chen, J. Wang, S. Ma and G. Ye, *Chem. Soc. Rev.*, 2023, **52**, 97–162.
6 Y. Yuan, T. Liu, J. Xiao, Q. Yu, L. Feng, B. Niu, S. Feng, J. Zhang and N. Wang, *Nat. Commun.*, 2020, **11**, 5708.
7 Y. Xu, Q. Liu, J. Zhu, H. Zhang, J. Liu, R. Chen, J. Yu, Y. Li and J. Wang, *Chem. Eng. J.*, 2022, **435**, 134958.
8 T. Chen, T. Liu, B. Pang, T. Ding, W. Zhang, X. Shen, D. Wu, L. Wang, X. Liu, Q. Luo, W. Zhu and T. Yao, *Sci. Bull.*, 2022, **67**, 2001–2012.
9 Q. Yang, J. Zhao, A. Muhammad, R. Qin, J. Tian, L. Li, Q. Zhang, L. Chen and P. Yang, *J. Mater. Chem. A*, 2022, **10**, 14906–14916.
10 J. Gan, L. Zhang, Q. Wang, Q. Xin, E. Hu, Z. Lei, H. Wang and H. Wang, *Desalination*, 2023, **545**, 116154.
11 B. Yan, C. Ma, J. Gao, Y. Yuan and N. Wang, *Adv. Mater.*, 2020, **32**, 1906615.
12 W.-R. Cui, F.-F. Li, R.-H. Xu, C.-R. Zhang, X.-R. Chen, R.-H. Yan, R.-P. Liang and J.-D. Qiu, *Angew. Chem., Int. Ed.*, 2020, **59**, 17684–17690.
13 C. Tsouris, *Nat. Energy*, 2017, **2**, 17047.
14 Y. Wang, Y. Wang, M. Song, S. Chen, J. Wei, J. You, B. Zhou and S. Wang, *Angew. Chem., Int. Ed.*, 2023, **62**, e202217601.
15 H. Yang, X. Liu, M. Hao, Y. Xie, X. Wang, H. Tian, G. I. N. Waterhouse, P. E. Kruger, S. G. Telfer and S. Ma, *Adv. Mater.*, 2021, **33**, 2106621.
16 L. Zhou, J. Lian, Q. Li, J. Li, Y. Shao, G. Wu, T. Ding, X. Cui, T. Chen and W. Zhu, *Inorg. Chem.*, 2023, **62**, 21518–21527.
17 C. Liu, P.-C. Hsu, J. Xie, J. Zhao, T. Wu, H. Wang, W. Liu, J. Zhang, S. Chu and Y. Cui, *Nat. Energy*, 2017, **2**, 17007.
18 J. Liao, X. He, Y. Zhang, L. Zhang and Z. He, *Chem. Eng. J.*, 2023, **457**, 141367.
19 Y. Zhang, B. Mei, B. Shen, L. Jia, J. Liao and W. Zhu, *Carbohydr. Polym.*, 2023, **312**, 120834.
20 J. Jian, H. Kang, D. Yu, X. Qiao, Y. Liu, Y. Li, W. Qin and X. Wu, *Small*, 2023, **19**, 2207378.
21 Y. Liao, R. Lei, X. Weng, C. Yan, J. Fu, G. Wei, C. Zhang, M. Wang and H. Wang, *J. Hazard. Mater.*, 2023, **442**, 130054.
22 H. Ye, T.-H. Li, Y.-Q. Huang, J.-M. Jin, J.-Y. Fei, M.-B. Wu and J. Yao, *Chem. Eng. J.*, 2023, **451**, 138615.
23 X. Liu, Y. Xie, M. Hao, Z. Chen, H. Yang, G. I. N. Waterhouse, S. Ma and X. Wang, *Advanced Science*, 2022, **9**, 2201735.
24 W. Sun, L. Feng, J. Zhang, K. Lin, H. Wang, B. Yan, T. Feng, M. Cao, T. Liu, Y. Yuan and N. Wang, *Advanced Science*, 2022, **9**, 2105008.
25 Y. Li, X. F. Lu, S. Xi, D. Luan, X. Wang and X. W. Lou, *Angew. Chem., Int. Ed.*, 2022, **61**, e202201491.
26 K. Wang, B. Chen, Y. Xuan, W. Fan, N. Sun, S. Chang and G. Meng, *Appl. Catal., B*, 2023, **338**, 123083.
27 N. Li, L. Yang, R. Su, N. Shi, J. Wu, J. Zhao, L. Wen and Z. Wang, *Desalination*, 2023, **566**, 116940.

28 S. Qi, S. Xiong, L. Xiong, H. Li, B. Liu, Y. Liu, K. Xiong, H. Yan, K. Lv, H. Liu and S. Hu, *Inorg. Chem.*, 2023, **62**, 10881–10886.
29 M. Li, R. Wang, T. Liu, Q. Chen, N. Li, L. Zhou, K. Yu, H. Liu, X. Gong, R. He, F. Ahmad, F. Yang, W. Zhu and T. Chen, *Sep. Purif. Technol.*, 2023, **309**, 123121.
30 Y. Ai, Y. Wang, L. Song, W. Hong, Z. Zhang, X. Li, S. Zhou and J. Zhou, *J. Hazard. Mater.*, 2023, **448**, 130965.
31 W. Wang, Q. Luo, L. Li, Y. Wang, X. Huo, S. Chen, X. Du and N. Wang, *Adv. Funct. Mater.*, 2023, **33**, 2302913.
32 Y. Fan, C. Zhuang, S. Li, Y. Wang, X. Zou, X. Liu, W. Huang and G. Zhu, *J. Mater. Chem. A*, 2021, **9**, 1110–1118.
33 Y. Xu, Z. Yao, Z. Mao, M. Shi, X. Zhang, F. Cheng, H. B. Yang, H. b. Tao and B. Liu, *Appl. Catal., B*, 2020, **277**, 119057.
34 T. Ding, X. Liu, Z. Tao, T. Liu, T. Chen, W. Zhang, X. Shen, D. Liu, S. Wang, B. Pang, D. Wu, L. Cao, L. Wang, T. Liu, Y. Li, H. Sheng, M. Zhu and T. Yao, *J. Am. Chem. Soc.*, 2021, **143**, 11317–11324.
35 C. Zhang, Z. Fu, Q. Zhao, Z. Du, R. Zhang and S. Li, *Electrochem. Commun.*, 2020, **116**, 106758.
36 L. Cao, I. K. M. Yu, D. C. W. Tsang, S. Zhang, Y. S. Ok, E. E. Kwon, H. Song and C. S. Poon, *Bioresour. Technol.*, 2018, **267**, 242–248.
37 E. Hu, Q. Chen, Q. Gao, X. Fan, X. Luo, Y. Wei, G. Wu, H. Deng, S. Xu, P. Wang, L. Liu, R. He, X. Chen, W. Zhu and Y. Zhu, *Adv. Funct. Mater.*, 2024, 2312215.
38 K. Yu, L. Tang, X. Cao, Z. Guo, Y. Zhang, N. Li, C. Dong, X. Gong, T. Chen, R. He and W. Zhu, *Adv. Funct. Mater.*, 2022, **32**, 2200315.
39 Y. He, W. Bao, Q. Du, X. Wu, X. Fu, D. Yuan, B. Na, F. Yu, S. Zhang, C. Peng and H. Liu, *Sep. Purif. Technol.*, 2024, **330**, 125448.
40 T. Chen, P. He, T. Liu, L. Zhou, M. Li, K. Yu, Q. Meng, J. Lian and W. Zhu, *Inorg. Chem.*, 2022, **61**, 12759–12771.
41 T. Chen, H. Dong, T. Liu, L. Zhou, D. Fu, B. Pang, J. Lian, T. Ding, W. Zhang, R. He and W. Zhu, *Inorg. Chem.*, 2023, **62**, 8615–8625.